Catalysis Science & Technology

ROYAL SOCIETY OF CHEMISTRY

PAPER

View Article Online
View Journal | View Issue

Check for updates

Cite this: *Catal. Sci. Technol.*, 2020, 10, 3279

Impact of edge structures on interfacial interactions and efficient visible-light photocatalytic activity of metal–semiconductor hybrid 2D materials†

Deobrat Singh, *[a] Pritam Kumar Panda,[a] Nabil Khossossi, [ab] Yogendra Kumar Mishra, [c] Abdelmajid Ainane[ab] and Rajeev Ahuja *[ad]

Received 3rd March 2020,
Accepted 21st April 2020

DOI: 10.1039/d0cy00420k

rsc.li/catalysis

The present work systematically investigates the structural, electronic, and optical properties of a MoS_2/Si_2BN heterostructure based on first-principles calculations. Firstly, the charge transport and optoelectronic properties of MoS_2 and Si_2BN heterostructures are computed in detail. We observed that the positions of the valence and conduction band edges of MoS_2 and Si_2BN change with the Fermi level and form a Schottky contact heterostructure with superior optical absorption spectra. Furthermore, the charge density difference profile and Bader charge analysis indicated that the internal electric field would facilitate the separation of electron–hole (e^-/h^+) pairs at the MoS_2/Si_2BN interface and restrain the carrier recombination. This work provides an insightful understanding about the physical mechanism for the better photocatalytic performance of this new material system and offers adequate instructions for fabricating superior Si_2BN-based heterostructure photocatalysts.

Introduction

In the contemporary era, massive challenges have been imposed on the research community to tackle environmental problems and look for renewable energy sources *i.e.* utilization of solar energy to obtain hydrogen and oxygen by water splitting. Hydrogen is a renewable and clean energy source and the mechanism to generate hydrogen and oxygen through photocatalytic water splitting bears significant challenges that include light harvesting, separation, migration of photogenerated electrons and holes, and the hydrogen evolution reaction (HER) and oxygen evolution reaction (OER) on the surface of photocatalysts. To achieve that, the redox potential of water must lie in between the conduction band minima (CBM) and valence band maxima (VBM), where the CBM should be higher than the reduction potential of H^+/H_2, and the VBM should be lower than the oxidation potential of H_2O/O_2. Moreover, the surface reactivities for the photocatalysts from the recombination of the irradiation-excited electrons and holes due to the adsorption of sunlight, finding narrow bandgap to dimensional (2D) materials for photocatalysis would be a significant challenge.[1]

2D semiconducting materials such as transition metal dichalcogenides (TMDs), metal chalcogenides (*e.g.*, MoS_2, WS_2), hexagonal boron nitrides (h-BNs), and metal oxides have garnered massive interest in experimental studies as well as theoretical studies due to their unique physical and chemical properties.[2–8] The challenges mentioned above can be easily handled with the band engineering of these semiconductors to develop catalysts with high photocatalysis performance.[9] The possibilities to explore the recent advances in van der Waals (vdW) solids of atomic layers that form vertical quantum heterojunctions with interfaces between different 2D materials. The in-plane stability of 2D materials induces strong covalent bonding. In contrast, the vdW interactions induce the stacking of different materials with diverse physical and chemical properties appearing to be appropriate for photocatalytic activity. Formation of heterostructures with dissimilar materials can have drastic effects on the photocatalytic activity due to the impact of the built-in electric field formed among the different layers, as reported earlier.[10] The proposed theoretical calculations represent the molecular mechanism for these stacking layers that may matter in deciding the net catalytic performance of

[a] *Department of Physics and Astronomy, Uppsala University, Box 516, Uppsala, Sweden. E-mail: deobrat.singh@physics.uu.se, rajeev.ahuja@physics.uu.se*
[b] *Laboratoire de Physique des Matèriaux et Modélisations des Systèmes, (LP2MS), Unité Associée au CNRST-URAC 08, Faculty of Sciences, Department of Physics, Moulay Ismail University, Meknes, Morocco*
[c] *NanoSYD, Mads Clausen Institute, University of Southern Denmark, Denmark*
[d] *Applied Materials Physics, Department of Materials and Engineering, Royal Institute of Technology (KTH), S-100 44 Stockholm, Sweden*

† Electronic supplementary information (ESI) available. See DOI: 10.1039/d0cy00420k

materials such as graphene and related 2D materials such as MoS_2, functionalized silicene and germanane, various MXenes (like Zr_2CO_2 and Hf_2CO_2), single layer group-III monochalcogenides and group-IVB nitride halides, SnS_2 with a tuned photocatalyst under acidic pH conditions, black phosphorene (Pn) with pseudo Jahn–Teller (PJT) effects buckled in a stapler-clip symmetry, black Pn under strain and heterostructures of h-BN/graphene.[11–22] The crystal structure of molybdenum disulfide (MoS_2) takes the form of a hexagonal plane of S atoms on either side of a hexagonal plane of Mo atoms. These triple planes stack on top of each other, with strong covalent bonds between the Mo and S atoms, but weak van der Waals forces holding the layers together. This allows them to be mechanically separated to form 2-dimensional sheets of MoS_2.[23,24] In the case of Si_2BN, it has a graphene-like structure by combining boron and nitrogen that leads to an sp^2-bonded single-layer hexagonal boron nitride (BN) structure, which is a wide-band-gap semiconductor with a bandgap of 5.8 eV.[25]

Van der Waals heterostructures are composite quantum materials consisting of arrays of two-dimensional (2D) layers, which are atomically thin as the electrons are exposed to layer-to-layer coupling in the atomically thin 2D layers.[26] The characteristics of van der Waals heterostructures are represented not only by the constituent monolayers but also by the interactions among the layers. Recently, various types of van der Waals heterostructures based on MoS_2 have exhibited several interesting electrical, optical, and magnetic properties,[27–39] but none has reported the mechanism of interface interactions (vdW heterostructures) between MoS_2 and Si_2BN. We have chosen a 2D Si_2BN (ref. 25) monolayer as a promising candidate as it possesses several characteristic features similar to those of graphene, *e.g.*, physical and mechanical robustness, a good degree of stability at high temperatures around 1000 K, high formation energy, ultra-high ideal strength, and unique electronic properties, making it suitable for optoelectronic, sensor, catalysis and nanoelectronic applications.[40] As the electrons in atomically thin layers (monolayers) are involved in stacking, forming a heterostructure, different quantum states found in the individual layers can interact and couple to one another. Heterostructures of 2D materials not only offer a way to research structural and electronic anomalies but also create unparalleled possibilities to incorporate them for technical use. Stacked monolayers are very different from traditional heterostructures of 3D semiconductors, since each layer functions concurrently as the bulk material and the interface, reducing the displacement charges within each sheet. Even charge transfers between layers can be very large, producing large electrical fields and providing fascinating band-structure engineering possibilities.[41] Surface reconstruction, charge transfer, and proximity effects (when one material can borrow the properties of another by contact *via* quantum tunneling or by Coulomb interactions) are some of the unique features that one can unravel by studying vdW heterostructures using various 2D materials.

In the present work, we mainly focused on the basic mechanism of interface interactions and charge movement and separation in and optical properties of a Si_2BN/MoS_2 heterostructure utilizing density functional theory (DFT) calculations. Our calculations demonstrate that after superimposing MoS_2 with a Si_2BN monolayer, the positions of the band edge of MoS_2 altered correspondingly, forming a semiconductor–metal heterostructure. The charge density differences, work function, and Bader charge analysis showed that the internal electric field between interfaces could further inhibit the recombination of e^-/h^+ pairs. Besides, we found that the optical absorption coefficient of the Si_2BN/MoS_2 heterostructure is more prominent than those of individual MoS_2 and Si_2BN under visible-light irradiation. We propose a productive methodology for the understanding of interfacial properties of Si_2BN/MoS_2 heterostructure with two different configurations: (i) monolayer of Si_2BN and MoS_2 system periodic in *XY* directions used as simple abbreviations $rMoS_2/Si_2BN$ and (ii) nanoribbon of MoS_2 system periodic in *x*-direction deposited on the monolayer of Si_2BN used as simple abbreviations $rMoS_2/Si_2BN$. Our investigation suggests the physicochemical system shows the photocatalytic activity of Si_2BN/MoS_2 hybrid heterostructure and envisages to design new hybrid heterostructures for photocatalytic responses.

Methodology

The electronic structure calculations are based on density functional theory (DFT) as implemented in the Vienna *ab initio* simulation package (VASP) software.[42–46] The projector augmented wave (PAW) method with generalized gradient approximation (GGA) in the form of the Perdew–Burke–Ernzerhof (PBE) exchange–correlation functional is a technique used in *ab initio* electronic structure calculations.[47–49] The effect of van der Waals interaction has been described by using the empirical correction in the Grimme method *i.e.*, zero damping DFT-D3 during the calculations.[50] The electron wave functions are described by a plane-wave basis set with a kinetic energy cutoff of 500 eV, and the convergence tolerance throughout the structure relaxation has been set to 10^{-6} eV for energy and 10^{-3} eV $Å^{-1}$ for force, respectively. A vacuum space of 20 Å in the *z*-direction has been used to prevent the physical interaction between two periodic images. The Brillouin zone (BZ) is sampled using a Monkhorst–Pack *K*-mesh grid of 6 × 6 × 1 for the supercell in the reciprocal space during the structural optimization.[51] The charge distribution and transfer are computed by using Bader charge analysis.[52] Additionally, *ab initio* molecular dynamics (MD) simulations were performed in the canonical ensemble *i.e.*, fixed particle number, volume, and temperature (NVT) up to 10 ps with a time step of 2 fs. To accelerate the dynamic process, we have used a temperature amounting to 300 K. The AIMD simulations have helped us to determine and examine the thermal stability of the MoS_2/Si_2BN vdW heterostructure. The optical absorption spectra have been extracted from the imaginary part of the

complex dielectric function, $\varepsilon(\omega) = \varepsilon_1(\omega) + \varepsilon_2(\omega)$, where $\varepsilon_1(\omega)$ is the real part and $\varepsilon_2(\omega)$ is the imaginary part of the complex dielectric function.[53] The optical absorption coefficient is given as:

$$\alpha = \sqrt{2}\omega[|\varepsilon(\omega)| - \varepsilon_1(\omega)]^{\frac{1}{2}}, \quad (1)$$

where,

$$|\varepsilon(\omega)| = \sqrt{\varepsilon_r{}^2(\omega) + \varepsilon_i{}^2(\omega)}$$

Results and discussion

The structures of the Si_2BN and MoS_2 monolayers are fully optimized and the corresponding lattice parameters $a = b = 3.18$ Å (bond lengths between the atoms of Mo–S = 2.41 Å and S–S = 3.13 Å) and $a = 6.35$ Å and $b = 6.45$ Å (bond lengths between the atoms of Si–Si = 2.25 Å, Si–B = 1.95 Å, Si–N = 1.76 Å, B–N = 1.47 Å) are well consistent with those from previously reported studies.[40,54–58] Here, we have fabricated the Si_2BN/MoS_2 heterostructure by combining a (2 × 2 × 1) supercell of the Si_2BN monolayer (which contains 16 Si, 8 N and 8 B atoms) and a (4 × 4 × 1) supercell of the MoS_2 monolayer (with 16 Mo and 32 S atoms). In case of $mMoS_2/Si_2BN$ heterostructure, the bottom of S atoms in MoS_2 monolayer has directly situated the top of Si_2BN monolayer as presented in Fig. 1(a). The interlayer van der Waals (vdW) interactions between the Si_2BN and MoS_2 monolayers will directly influence the structural stability and electronic properties of the heterostructure interface. In this case, we have considered the possible minimum energy configuration structure. Initially, we have fabricated a 3.54 Å vertical distance between the Si_2BN and MoS_2 monolayers for the interfacial vdW interactions and the corresponding relative energy profile is presented in Fig. S1 (see the ESI†). Due to the strong vdW interactions in the heterostructure, the vertical distance is reduced from 3.54 Å to 2.99 Å. For the structural lattice mismatch, we have increased the size of the unit cell of both Si_2BN (1 × 1 × 1 to a 2 × 2 × 1 supercell) and MoS_2 (1 × 1 × 1 to a 4 × 4 × 1 supercell) monolayers and it is defined by $\Delta a = \left(\frac{|a_{Si_2BN} - a_{MoS_2}|}{a_{Si_2BN}}\right) \times 100$, where a_{Si_2BN} is the lattice parameter of the Si_2BN monolayer and a_{MoS_2} is the lattice parameter of the MoS_2 monolayer. The calculated values of lattice mismatch Δa in the direction of a and b are 0.1% and 1.4%, which is in the a direction negligible and in the b direction acceptable, respectively.

After the optimization of the crystal structure, no structural distortion is found which is very similar to a previously studied graphene/MoS_2 interface.[59] The vertical distance between the Si_2BN and MoS_2 monolayers are 2.99 Å and 2.20 Å for $mMoS_2/Si_2BN$ and $rMoS_2/Si_2BN$, respectively and it shows the vdW equilibrium spacing. The S atoms of MoS_2 monolayer shows only physisorption interactions. For the thermodynamic stability of the physical interaction between the Si_2BN and MoS_2 monolayers, we have calculated the adhesion energy as follows:

$$E_{ad} = E_{Si_2BN/MoS_2} - E_{Si_2BN} - E_{MoS_2} \quad (2)$$

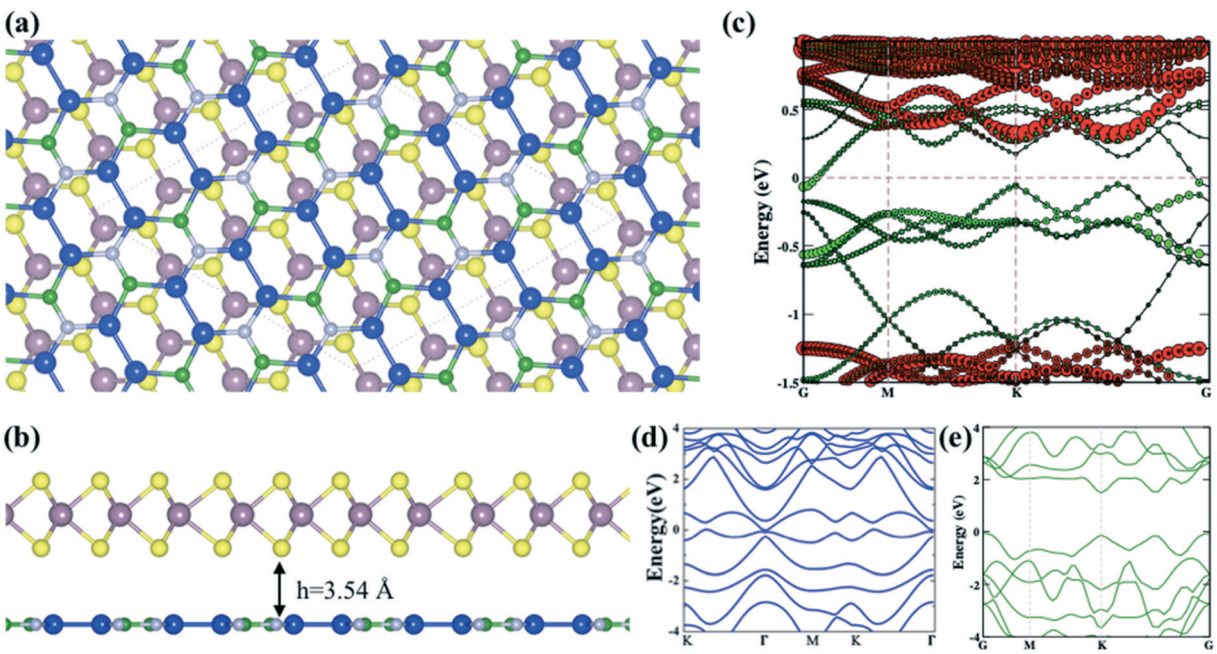

Fig. 1 The optimized $mMoS_2/Si_2BN$ heterostructure viewed from the (a) top and (b) side and the (c) corresponding band structure (green and red colors represent the electronic band lines of Si_2BN and MoS_2, respectively). The electronic band structures of pristine (d) Si_2BN and (e) MoS_2 monolayers.

where E_{Si_2BN/MoS_2}, E_{Si_2BN}, and E_{MoS_2} represent the total energy of the heterostructure, pristine Si_2BN monolayer, and pristine MoS_2 monolayer, respectively. With vdW interactions between the Si_2BN and MoS_2 monolayers, we found an adhesion energy E_{ad} of −5.23 eV (≈−36 meV Å^{-2}) and −10.24 eV (≈−71 meV Å^{-2}) for $mMoS_2/Si_2BN$ and $rMoS_2/Si_2BN$, respectively, which are lower than that of the previously reported graphene/MoS_2 heterostructure,[60] which is the energetically most favorable vdW heterostructure. The interfacial contact between the Si_2BN and MoS_2 monolayers may be a unique feature for its future applications as photocatalytic activity.

To understand the electronic properties of the $mMoS_2/Si_2BN$ heterostructure, we have calculated the atom-decomposed electronic band structure as presented in Fig. 1(c). For the comparison of the electronic band structure of $mMoS_2/Si_2BN$, we have also computed the individual band structures of the Si_2BN and MoS_2 monolayers as shown in Fig. 1(d) and (e), respectively. From the electronic band structure of heterostructure, we can see that the electronic band lines slightly changes at high symmetry points and opens the direct bandgap at Γ and K points as presented in Fig. 1(c). The computed electronic band structure shows the metallic behavior of the Si_2BN monolayer as presented in Fig. 1(d). Additionally, the calculated band structure of the MoS_2 monolayer shows a direct bandgap of 1.64 eV from the valence band maximum, and the conduction band minimum is located at the K-point as shown in Fig. 1(e). The value of the theoretical bandgap 1.64 eV is underestimated compared with the experimental bandgap 1.8 eV.[61] During the contact of Si_2BN with MoS_2 monolayer reduced the bandgap 1.43 eV from 1.64 eV and the Fermi level-shifted towards the conduction band minimum side; due to this, it shows n-type behavior. Also, one band line crosses the Fermi level at the Γ point of the Si_2BN monolayer and the electronic band lines are separated as compared to the pristine case at the Γ point as shown in Fig. 1(c). Predominantly, the metallic conductivity in the complex system is mediated by the Si_2BN surface.

Previous investigations suggested that the stability of the MoS_2 nanoribbon is strongly dependent on edge structures in which the sulphur terminated edges (zigzag direction) had the lowest energy configuration.[60,62,63] In the present work, we have mounted the MoS_2 nanoribbon on the monolayer surface of Si_2BN in which the MoS_2 nanoribbon has S atoms on one terminal edge and Mo atoms on the other edge as presented in Fig. 2(a). In the case of $rMoS_2/Si_2BN$, the lateral separation distance between nanoribbon MoS_2 and its periodic images is 15 Å to prevent physical interactions. The fully optimized structural configuration has slight distortion at the nanoribbon edges which is consistent with the previous literature.[60,62,63]

Furthermore, we have calculated the projected density of states (PDOS) of the pristine Si_2BN and MoS_2 monolayers as well as the $mMoS_2/Si_2BN$ and $rMoS_2/Si_2BN$ heterostructures as shown in Fig. S3.† From the electronic density of states of pristine Si_2BN, the monolayer has more contribution from the Si-p orbital and a small contribution comes from the p-orbitals of the B and N atoms at the Fermi level as shown in Fig. S3(a).† Due to the presence of some electronic states at the Fermi level, pristine Si_2BN shows metallic behavior. But in the case of the pristine MoS_2 monolayer, the electronic states are dominated by the d-orbital of Mo atoms and a very small contribution comes from the S p-orbital near the Fermi level in both the VBM and CBM as presented in Fig. S3(b).† We can see that the pristine MoS_2 monolayer shows p-type semiconducting behavior (see Fig. 1e and S3b†). Furthermore, with the interfacial contact between Si_2BN and MoS_2, the heterostructure ($mMoS_2/Si_2BN$) shows metallic behavior in which the p-orbital of Si atoms is responsible for band crossing at the Fermi level. Also, the electronic states of MoS_2 shifted towards the CBM side due to the significant vdW interactions between the Si_2BN and MoS_2 monolayers. According to this, the Si_2BN and MoS_2 monolayers behave like n-type semiconductors with the contact of the Si_2BN surface. There are no significant changes in the electronic states of the Si_2BN monolayer because it shows metallic

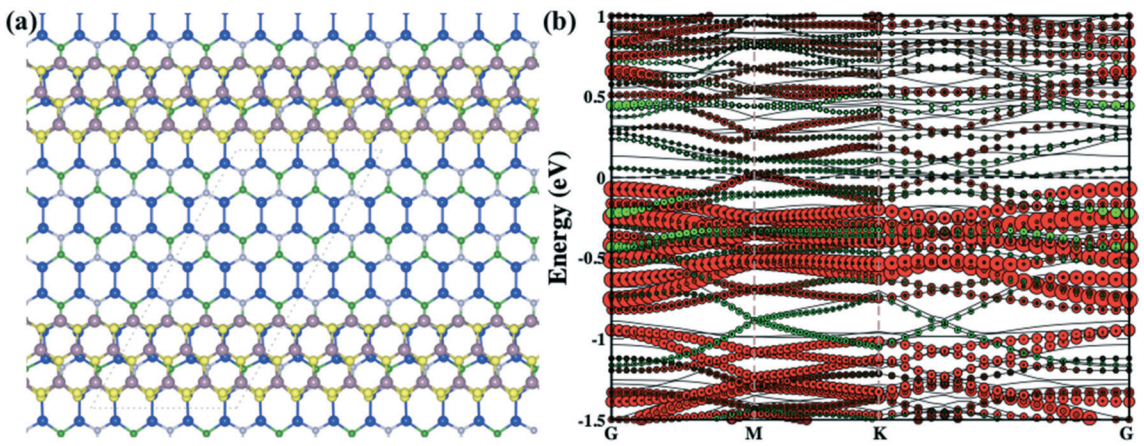

Fig. 2 The optimized $rMoS_2/Si_2BN$ heterostructure (a) and the corresponding band structure (b) (green and red colors represent the electronic band lines of Si_2BN and MoS_2, respectively).

behavior before and after the contact with the MoS_2 monolayer. Moreover, during the interfacial contact between a monolayer of Si_2BN and MoS_2 shows metallic nature for both vdW heterostructure $mMoS_2/Si_2BN$ and $rMoS_2/Si_2BN$. But in this case, the p-orbital of the Si atoms is strongly hybridized with the d-orbital of the Mo atoms, which appears near and at the Fermi level, as shown in Fig. 2(b) and S3(d).† The terminal edge S and Mo atoms of the MoS_2 nanoribbon may be a more reactive surface with the Si_2BN monolayer and this is why lots of electronic band lines cross the Fermi level in the electronic band structures.

Charge distribution and work function studies

The entirely distinct electronic properties of both $mMoS_2/Si_2BN$ and $rMoS_2/Si_2BN$ heterostructures are induced by the different termination of the MoS_2 surface, mainly the existence of edge atoms of the MoS_2 nanoribbon. The effect of the MoS_2 edges is determined by the charge density difference plot. The charge density difference plot is calculated by:

$$\Delta\rho = \rho Si_2BN/MoS_2 - \rho Si_2BN - \rho MoS_2, \quad (3)$$

where ρSi_2BN and ρMoS_2 are the electron density of isolated Si_2BN and MoS_2 systems, respectively, and $\rho Si_2BN/MoS_2$ is the electron density of a $mMoS_2/Si_2BN$ or $rMoS_2/Si_2BN$ complex system. The electron charge density difference plots are depicted in Fig. 3. In the case of the $mMoS_2/Si_2BN$ heterostructure, electron transfer is detected because we can see that a significant electron cloud is present at the interface. Both cases have significant electron clouds at the interface of the heterostructure. But in the case of $mMoS_2/Si_2BN$ heterostructure, the charge transfer between MoS_2 and Si_2BN is relatively less as compared to $rMoS_2/Si_2BN$ heterostructure, as shown in Fig. 3(a and b). The charge transfer is consistent with adhesion energy that is a physical interaction between monolayer MoS_2 on Si_2BN is relatively half as compared to nanoribbon MoS_2 on the Si_2BN system. It is observed that excess electrons accumulate at the S-edge of the MoS_2 monolayer and MoS_2 ribbon. Due to the edge-effect of nanoribbon MoS_2, it has more electron clouds at the S-edge. This phenomenon is also observed in $rMoS_2/Si_2BN$, as demonstrated in Fig. 3b, as the clouds that represent electron accumulation spread systematically over the MoS_2 nanoribbon. The accumulation of electrons at the MoS_2 surface would be important for the edge atoms to act as active sites in catalysis. It was experimentally reported that the presence of edge atoms in the MoS_2 system in the case of the MoS_2/graphene heterostructure causes it to have high activities for catalysis and potential applications for sensing and energy storage devices.[59,60,64–67] Our findings also suggest that the edge states are responsible for enhancing the charge-transport properties.

Additionally, we have calculated the planar averaged charge density difference along the *z*-direction, as shown in Fig. 4(a and b). The positive value on the *y*-axis indicates electron accumulation and the negative value on the *y*-axis indicates electron depletion. It is noticed that the electron transfer occurs from the Si_2BN monolayer to the MoS_2 surface in the heterostructure appearing at the interface

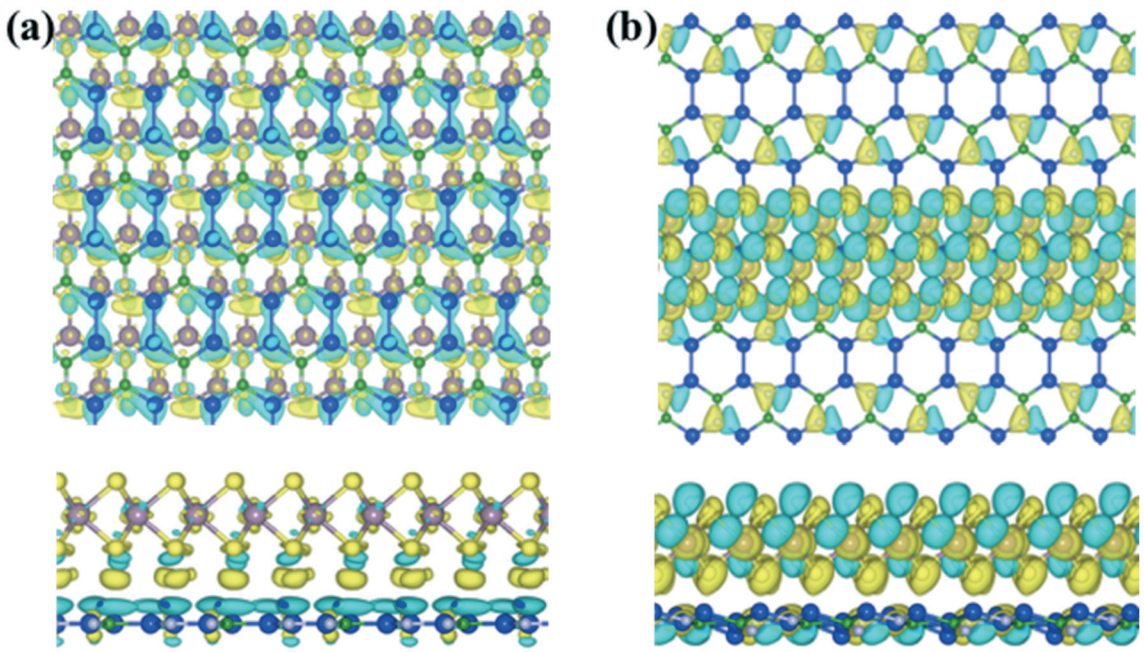

Fig. 3 Top view (upper panel) and side view (lower panel) of the electron density difference plots for the (a) $mMoS_2/Si_2BN$ and (b) $rMoS_2/Si_2BN$ heterostructures. The iso-value is set as 10^{-3} e Å^{-3}. The cyan and yellow colors represent the charge depletion and accumulation in space, respectively.

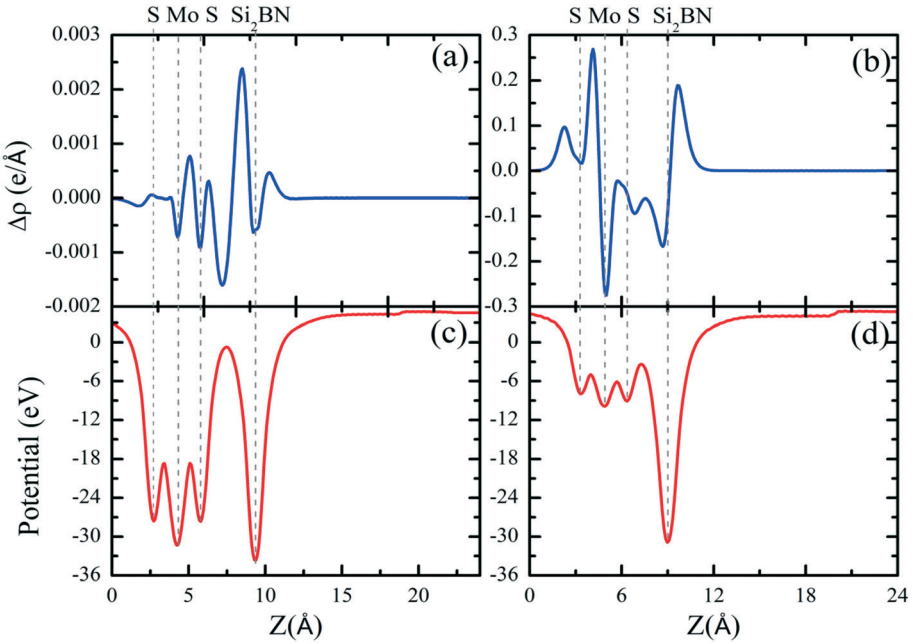

Fig. 4 Planar-averaged electron density differences $\Delta\rho(z)$ for the (a) $mMoS_2/Si_2BN$ and (b) $rMoS_2/Si_2BN$ heterostructures. The electrostatic potentials for the (c) $mMoS_2/Si_2BN$ and (d) $rMoS_2/Si_2BN$ heterostructures.

region. To quantify the amount of charge transferred, we have used Bader charge analysis for such an interfacial interaction surface. We found that the monolayer Si_2BN transfers 0.122 e^- and 0.553 e^- to the monolayer and nanoribbon MoS_2, respectively. This phenomenon can be easily understood by analyzing the electrostatic potential and corresponding simulated work function of the pristine MoS_2 and Si_2BN monolayers, as presented in Fig. 4(c and d) and 5. The work functions of the pristine MoS_2 and Si_2BN monolayers are 5.82 eV and 4.32 eV, respectively. However, the $mMoS_2/Si_2BN$ and $rMoS_2/Si_2BN$ heterostructures have work functions situated between those of the pristine MoS_2 and Si_2BN layers. This means that the significant changes in the electrostatic potential regulate the charge redistribution in the heterostructure system. According to that, spontaneous interfacial electron transfer occurs from the Si_2BN layer to the MoS_2 layer, which is easily justified in terms of the large difference in work functions. It is also known that the electrons transfer from a lower potential region to a higher potential region.[68] Due to the significant charge transfer at the interfacial region, an internal electric field is generated which can effectively enhance the photogenerated electron–hole (e^-/h^+) pair separation between the MoS_2 and Si_2BN layers. In previous investigations, it was found that a similar charge redistribution occurred in hybrid MoS_2/graphene[60] and black phosphorus/$BiVO_4$.[68]

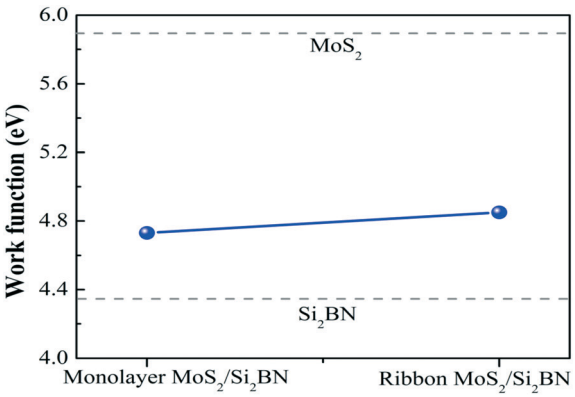

Fig. 5 Work functions of $mMoS_2/Si_2BN$ and $rMoS_2/Si_2BN$. The dotted lines for pristine MoS_2 and Si_2BN are also shown for comparison.

Mechanism of photocatalytic activity

For the purpose of exploring in detail the regioselectivity of hydrogen atoms, the binding characteristics on different sides of both MoS_2/Si_2BN heterostructures (monolayer and ribbon) were explored in our calculations. Fig. 6(a–d) shows the top and side views of $mMoS_2/Si_2BN$ and $rMoS_2/Si_2BN$ with a H-atom adsorbed on either the MoS_2-side or Si_2BN-side. To get a better understanding of the favorable binding sites on both sides of $mMoS_2/Si_2BN$ and $rMoS_2/Si_2BN$, distinct binding sites were examined. In the case of the Si_2BN-side, the sites were located above the B, N, and Si atoms and Si–Si, B–N, N–Si, and Si–Si bridges, and hollow sites. In the case of the MoS_2-side, four kinds of binding sites were considered, in which the first one is located above the Mo-atoms, the second is above the S-atoms, the third is between the Mo–S bonds and the last one is at the hollow site of the hexagons that contain 3Mo- and 3S-atoms. The summarized adsorption energies at the most stable binding sites for an H-atom adsorbed on both sides are described in Table 1. It is obvious from this table that the adsorption process of a H-atom on

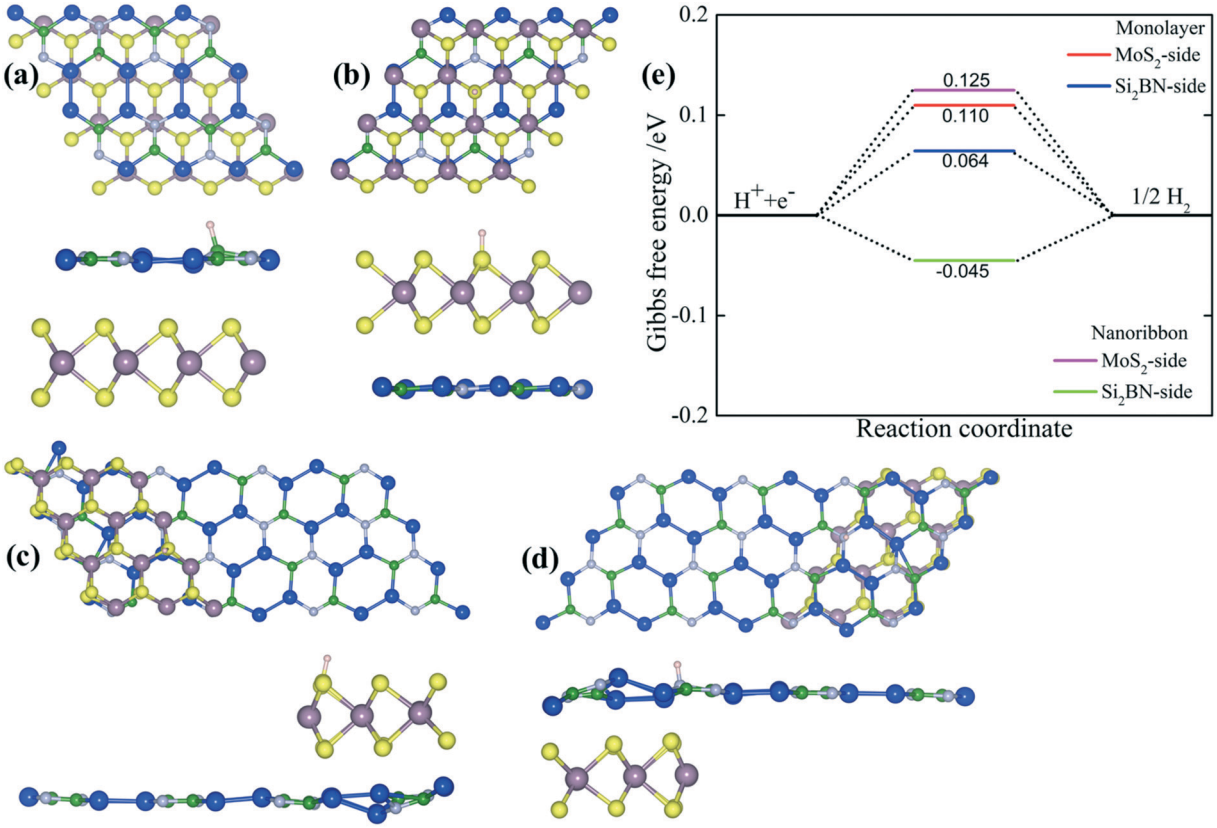

Fig. 6 (a–d) Top and side views of monolayer and ribbon MoS_2/Si_2BN with a hydrogen atom adsorbed at the most favorable site on both sides. (e) Calculated Gibbs free energy profile for the hydrogen evolution reaction (HER) on both sides of monolayer MoS_2/Si_2BN and ribbon MoS_2/Si_2BN.

Table 1 The adsorption energies of a H-atom E_{ad} (eV) adsorbed on the most stable binding site and the adsorption free energies (ΔG_{H^*}) on both sides of $mMoS_2/Si_2BN$ and $rMoS_2/Si_2BN$ (see Fig. 6a–d). Bader charge analysis of a hydrogen atom on the MoS_2- and Si_2BN-sides of both heterostructures, monolayer MoS_2/Si_2BN and ribbon MoS_2/Si_2BN

	E_a (eV)		ΔG_{H^*} (eV)		Bader analysis	
Systems	MoS_2-Side	Si_2BN-Side	MoS_2-Side	Si_2BN-Side	MoS_2-Side	Si_2BN-Side
Monolayer MoS_2	−0.13	−0.115	0.11	0.125	0.056	0.14
Ribbon MoS_2	−0.176	−0.285	0.064	−0.045	0.062	0.99

$rMoS_2/Si_2BN$ is better than that on $mMoS_2/Si_2BN$, with the adsorption energy being −0.176 eV in the case of the MoS_2-side and −0.285 eV in the case of the Si_2BN-side. The thermodynamic stability of the MoS_2/Si_2BN vdW heterostructure at 300 K was investigated by *ab initio* molecular dynamics (MD) simulations based on the Nose thermostat algorithm. The evolution of the total potential energy with simulation time and the final snapshot after 10 ps are shown in Fig. S4.† The total energies at 300 K remain almost invariant during the simulation. One can see in Fig. S4† that the final energy fluctuations tend to smoothen in the energy range up to 3 eV for $mMoS_2/Si_2BN$ and 5 eV for $rMoS_2/Si_2BN$. Our results indicate that the honeycomb network of the MoS_2 and Si_2BN regions remain unchanged which led to a stable structure with no breaking of bonds, basically, under 300 K. MD simulations suggest that the MoS_2/Si_2BN vdW heterostructure is thermally stable at 300 K.

To gain insight into the adsorption mechanisms, the adsorption free energy (ΔG_{H^*}) in the different sides of both heterostructures was also calculated, as illustrated in Table 1 and Fig. 6e. Generally, a potential catalyst with a better and efficient HER activity should be characterized by zero adsorption free energy ($\Delta G_{H^*} \rightarrow 0$). It is noted that the adsorption free energies are near zero in the case of $rMoS_2/Si_2BN$ with about −0.045 eV and −0.062 eV when hydrogen is adsorbed on the MoS_2-side and Si_2BN-side, respectively, which is better compared to $mMoS_2/Si_2BN$ with ΔG_{H^*a} of about 0.11 eV and 0.125 eV for the MoS_2-side and Si_2BN-side, respectively. Consequently, the hydrogen evolution reaction activity in the case of ribbon MoS_2/Si_2BN is ideal compared to that of the monolayer MoS_2/Si_2BN. As previously reported, the Gibbs free energy on the pristine MoS_2 and Si_2BN monolayers were found to be 1.29–1.80 eV (ref. 60) and 0.122 eV (ref. 54), respectively.

To further quantify this detail, the charge transfer mechanism was evaluated by Bader charge analysis to consider the distribution of charge when an H-atom is adsorbed on the different sides of the MoS_2/Si_2BN heterostructures. In the case of a hydrogen atom adsorbed either on the MoS_2-side or Si_2BN-side of $mMoS_2/Si_2BN$, the hydrogen gains a net amount of charge of 0.056 $|e|$ and 0.014 $|e|$, respectively, and when a hydrogen atom is adsorbed either on the MoS_2-side and Si_2BN-side of $rMoS_2/Si_2BN$, the hydrogen atom gains a charge of 0.062 $|e|$ and 0.99 $|e|$, respectively, indicating that the charge transfer mechanism arises through the MoS_2- and Si_2BN-sides of the heterostructures to the H-atom.

Based on the above-mentioned results of work function, Fig. 7 shows the activity of MoS_2/Si_2BN for photocatalytic water splitting, which is explored by comparing the band positions of MoS_2 and Si_2BN before and after contact to the reduction and oxidation potentials. The Fermi level of MoS_2 before contact is very close to the VB, and that of Si_2BN is located near the CB. Furthermore, the Fermi level equilibration leads to the generation of an internal electric field and hence charge diffusion; this, in turn, shifts the band positions of MoS_2. Thus, the energy levels of MoS_2 shift upward along with the Fermi level, whereas those of Si_2BN shift downward along with the Fermi level until the Fermi level of MoS_2 and Si_2BN reach an equilibrium; this leads to the generation of an internal electric field with a negatively charged portion at the interface of the MoS_2 region and a positively charged portion at the interface of the Si_2BN region. On the other hand, by definition, the CBM must be situated above the H^+/H_2 reduction potential (0 V *vs.* NHE), while the VBM must be located below the O_2/H_2O oxidation potential (1.23 V *vs.* NHE). In the case of before contact, the CBM potential of MoS_2 is −0.33 eV lower than the reduction potential of H^+/H_2, while the VBM potential is 0.08 eV higher than the oxidation potential of O_2/H_2O, which is sufficient for oxidation and reduction of water considering the overpotential factor. After contact, the relative positions of the CBM and VBM of MoS_2 will change with the Fermi level due to the charge redistribution. The CBM potential (about −0.84 eV) becomes much lower than the reduction potential of H^+/H_2, while the VBM potential (0.80 eV) of MoS_2 becomes −0.43 eV lower than the oxidation potential of O_2/H_2O.

The optical absorption spectra is an important factor in describing the performance of the photocatalyst of vdW heterostructures for photocatalytic activities. Thus, the absorption spectra of the fully optimized pristine MoS_2 and Si_2BN monolayers, as well as the heterostructures $mMoS_2/Si_2BN$ and $rMoS_2/Si_2BN$, were studied by computing the imaginary component of the complex dielectric function as illustrated in Fig. 8. According to the computed absorption coefficients in the visible light range between 1.55 eV and 3.1 eV, the Si_2BN monolayer scarcely absorbs visible light compared to MoS_2, which displays a significant absorption capacity. However, in the case of the MoS_2/Si_2BN heterostructures, the optical absorption of $mMoS_2/Si_2BN$ is significantly greater compared to that of $rMoS_2/Si_2BN$ and the Si_2BN monolayer but is slightly less than that of the MoS_2 monolayer. These indicate the promising application of the $mMoS_2/Si_2BN$ heterostructure as a great light absorber.

Conclusions

In summary, the effects of MoS_2 edge structure on the electronic structures, charge transport, and work functions of MoS_2/Si_2BN heterostructures have been investigated using first-principles calculations. The interfacial interactions between edge-free MoS_2 and a Si_2BN monolayer are weak vdW interactions which do not affect the properties of Si_2BN and the semiconducting behavior of the MoS_2 monolayer; however, the Fermi level is shifted towards the conduction band side (n-type semiconductor conductivity) in the case of the MoS_2 monolayer. When MoS_2 has exposed edges, the MoS_2 ribbon on a Si_2BN monolayer in the current study, the binding strength and electronic coupling at the interface are enhanced, resulting in more electrons transferred from the Si_2BN surface to the MoS_2 nanoribbon surface which can

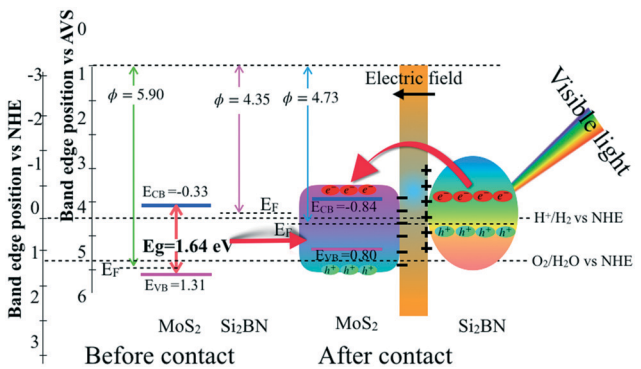

Fig. 7 A schematic diagram of the band configuration and the charge separation at the interface of MoS_2/Si_2BN under visible-light irradiation.

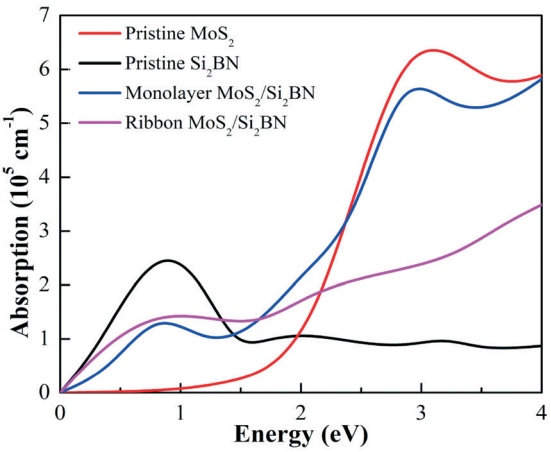

Fig. 8 Optical absorption spectra of the pristine MoS_2 monolayer, Si_2BN monolayer, $mMoS_2/Si_2BN$, and $rMoS_2/Si_2BN$, represented by red, black, blue, and magenta lines, respectively.

effectively enhance the photogenerated electron–hole pair separation between the MoS_2 and Si_2BN nanosheets. Additionally, the excess electrons at the MoS_2 surface are chemically more active, which can be used for energy storage and gas sensing applications. The electronic properties of MoS_2/Si_2BN heterostructures is strongly influenced by the MoS_2 dimensions, which could be potential materials for nanoelectronic devices and catalytic materials.

Conflicts of interest

There are no conflicts to declare.

Acknowledgements

The authors thank Olle Engkvists Stiftelse and the Swedish Research Council (VR) for financial support. AA acknowledges the PPR2 project (MISTERSFC-CNRST) for providing financial support. SNIC and HPC2N are acknowledged for providing the computing facilities.

References

1 K. Xiong, *et al.* Functional Group Effects on the Photoelectronic Properties of MXene (Sc2CT2, T = O, F, OH) and Their Possible Photocatalytic Activities, *Sci. Rep.*, 2017, **7**, 15095.

2 K. Pandey, *et al.* First step to investigate nature of electronic states and transport in flower-like MoS2: Combining experimental studies with computational calculations, *Sci. Rep.*, 2016, **6**, 32690.

3 D. Singh, S. K. Gupta, Y. Sonvane, A. Kumar and R. Ahuja, 2D-HfS 2 as an efficient photocatalyst for water splitting, *Catal. Sci. Technol.*, 2016, **6**, 6605–6614.

4 D. Singh, N. Singh, S. K. Gupta and Y. Sonvane, Effect on electronic and optical properties of Frenkel and Schottky defects in HfS2 monolayer, *AIP Conf. Proc.*, 2018, 090023, DOI: 10.1063/1.5028938.

5 D. Singh and R. Ahuja, Enhanced Optoelectronic and Thermoelectric Properties by Intrinsic Structural Defects in Monolayer HfS 2, *ACS Appl. Energy Mater.*, 2019, **2**, 6891–6903.

6 B. Radisavljevic, A. Radenovic, J. Brivio, V. Giacometti and A. Kis, Single-layer MoS2 transistors, *Nat. Nanotechnol.*, 2011, **6**, 147–150.

7 C. Tsai, F. Abild-Pedersen and J. K. Nørskov, Tuning the MoS 2 Edge-Site Activity for Hydrogen Evolution via Support Interactions, *Nano Lett.*, 2014, **14**, 1381–1387.

8 G. Ye, *et al.* Defects Engineered Monolayer MoS 2 for Improved Hydrogen Evolution Reaction, *Nano Lett.*, 2016, **16**, 1097–1103.

9 C.-F. Fu, X. Wu and J. Yang, Material Design for Photocatalytic Water Splitting from a Theoretical Perspective, *Adv. Mater.*, 2018, **30**, 1802106.

10 R. K. Biroju, *et al.* Hydrogen Evolution Reaction Activity of Graphene–MoS 2 van der Waals Heterostructures, *ACS Energy Lett.*, 2017, **2**, 1355–1361.

11 C. Chowdhury, S. Karmakar and A. Datta, Monolayer Group IV–VI Monochalcogenides: Low-Dimensional Materials for Photocatalytic Water Splitting, *J. Phys. Chem. C*, 2017, **121**, 7615–7624.

12 D. Voiry, *et al.* The role of electronic coupling between substrate and 2D MoS2 nanosheets in electrocatalytic production of hydrogen, *Nat. Mater.*, 2016, **15**, 1003–1009.

13 J. Yan, *et al.* Construction of a 2D Graphene-Like MoS 2 /C 3 N 4 Heterojunction with Enhanced Visible-Light Photocatalytic Activity and Photoelectrochemical Activity, *Chem. – Eur. J.*, 2016, **22**, 4764–4773.

14 S. Bawari, T. N. Narayanan and J. Mondal, Atomistic Elucidation of Sorption Processes in Hydrogen Evolution Reaction on a van der Waals Heterostructure, *J. Phys. Chem. C*, 2018, **122**, 10034–10041.

15 F. A. Frame and F. E. Osterloh, CdSe-MoS 2 : A Quantum Size-Confined Photocatalyst for Hydrogen Evolution from Water under Visible Light, *J. Phys. Chem. C*, 2010, **114**, 10628–10633.

16 Z. Li, X. Meng and Z. Zhang, Recent development on MoS2-based photocatalysis: A review, *J. Photochem. Photobiol., C*, 2018, **35**, 39–55.

17 D. Lu, *et al.* Highly Efficient Visible-Light-Induced Photoactivity of Z-Scheme g-C 3 N 4 /Ag/MoS 2 Ternary Photocatalysts for Organic Pollutant Degradation and Production of Hydrogen, *ACS Sustainable Chem. Eng.*, 2017, **5**, 1436–1445.

18 E. Parzinger, *et al.* Photocatalytic Stability of Single- and Few-Layer MoS 2, *ACS Nano*, 2015, **9**, 11302–11309.

19 S. Min and G. Lu, Sites for High Efficient Photocatalytic Hydrogen Evolution on a Limited-Layered MoS 2 Cocatalyst Confined on Graphene Sheets—The Role of Graphene, *J. Phys. Chem. C*, 2012, **116**, 25415–25424.

20 W. Gao, M. Wang, C. Ran and L. Li, Facile one-pot synthesis of MoS 2 quantum dots–graphene–TiO 2 composites for highly enhanced photocatalytic properties, *Chem. Commun.*, 2015, **51**, 1709–1712.

21 Y.-F. Zhao, *et al.* Cu 2 O Decorated with Cocatalyst MoS 2 for Solar Hydrogen Production with Enhanced Efficiency under Visible Light, *J. Phys. Chem. C*, 2014, **118**, 14238–14245.

22 W. Peng and X. Li, Synthesis of MoS2/g-C3N4 as a solar light-responsive photocatalyst for organic degradation, *Catal. Commun.*, 2014, **49**, 63–67.

23 K. F. Mak, C. Lee, J. Hone, J. Shan and T. F. Heinz, Atomically Thin <math display="inline"> <msub> <mi>MoS</mi> <mn>2</mn> </msub> </math> : A New Direct-Gap Semiconductor, *Phys. Rev. Lett.*, 2010, **105**, 136805.

24 P. Joensen, R. F. Frindt and S. R. Morrison, Single-layer MoS2, *Mater. Res. Bull.*, 1986, **21**, 457–461.

25 A. N. Andriotis, E. Richter and M. Menon, Prediction of a new graphenelike <math> <mrow> <msub> <mi>Si</mi> <mn>2</mn> </msub> <mi>BN</mi> </mrow> </math> solid, *Phys. Rev. B*, 2016, **93**, 081413.

26 C. Jin, *et al.* Ultrafast dynamics in van der Waals heterostructures, *Nat. Nanotechnol.*, 2018, **13**, 994–1003.

27 W. Yang, *et al.* Interlayer interactions in 2D WS 2 /MoS 2 heterostructures monolithically grown by in situ physical vapor deposition, *Nanoscale*, 2018, **10**, 22927–22936.
28 M. Zhao, *et al.* Interlayer coupling in anisotropic/isotropic van der Waals heterostructures of ReS2 and MoS2 monolayers, *Nano Res.*, 2016, **9**, 3772–3780.
29 S. Wang, X. Wang and J. H. Warner, All Chemical Vapor Deposition Growth of MoS 2 :h-BN Vertical van der Waals Heterostructures, *ACS Nano*, 2015, **9**, 5246–5254.
30 X. Zhou, *et al.* Vertical heterostructures based on SnSe 2 / MoS 2 for high performance photodetectors, *2D Mater.*, 2017, **4**, 025048.
31 F. Wang, *et al.* Tuning Coupling Behavior of Stacked Heterostructures Based on MoS2, WS2, and WSe2, *Sci. Rep.*, 2017, **7**, 44712.
32 Z. Huang, *et al.* Band structure engineering of monolayer MoS 2 on h-BN: first-principles calculations, *J. Phys. D: Appl. Phys.*, 2014, **47**, 075301.
33 Y. P. Venkata Subbaiah, K. J. Saji and A. Tiwari, Atomically Thin MoS 2 : A Versatile Nongraphene 2D Material, *Adv. Funct. Mater.*, 2016, **26**, 2046–2069.
34 J.-W. Jiang, Graphene versus MoS2: A short review, *Front. Phys.*, 2015, **10**, 287–302.
35 S. Bertolazzi, D. Krasnozhon and A. Kis, Nonvolatile Memory Cells Based on MoS 2 /Graphene Heterostructures, *ACS Nano*, 2013, **7**, 3246–3252.
36 W. Zhou, *et al.* Synthesis of Few-Layer MoS 2 Nanosheet-Coated TiO 2 Nanobelt Heterostructures for Enhanced Photocatalytic Activities, *Small*, 2013, **9**, 140–147.
37 Y. Li, C.-Y. Xu, J.-Y. Wang and L. Zhen, Photodiode-Like Behavior and Excellent Photoresponse of Vertical Si/ Monolayer MoS2 Heterostructures, *Sci. Rep.*, 2015, **4**, 7186.
38 H. Fang, *et al.* Strong interlayer coupling in van der Waals heterostructures built from single-layer chalcogenides, *Proc. Natl. Acad. Sci. U. S. A.*, 2014, **111**, 6198–6202.
39 M.-H. Chiu, *et al.*, Determination of band alignment in the single-layer MoS2/WSe2 heterojunction, *Nat. Commun.*, 2015, **6**, 7666.
40 D. Singh, S. K. Gupta, Y. Sonvane, T. Hussain and R. Ahuja, Achieving ultrahigh carrier mobilities and opening the band gap in two-dimensional Si 2 BN, *Phys. Chem. Chem. Phys.*, 2018, **20**, 21716–21723.
41 K. S. Novoselov, A. Mishchenko, A. Carvalho and A. H. Castro Neto, 2D materials and van der Waals heterostructures, *Science*, 2016, **353**, aac9439.
42 P. Blanchard and E. Brüning, Density Functional Theory of Atoms and Molecules, in *Progress in Mathematical Physics*, 2015, pp. 563–573, DOI: 10.1007/978-3-319-14045-2_37.
43 L. J. Bartolotti and K. Flurchick, An Introduction to Density Functional Theory, in *Reviews in Computational Chemistry*, 2007, pp. 187–216, DOI: 10.1002/9780470125847.ch4.
44 G. Kresse and J. Furthmüller, Efficient iterative schemes for ab initio total-energy calculations using a plane-wave basis set, *Phys. Rev. B: Condens. Matter Mater. Phys.*, 1996, **54**, 11169–11186.
45 W. Kohn, Density Functional and Density Matrix Method Scaling Linearly with the Number of Atoms, *Phys. Rev. Lett.*, 1996, **76**, 3168–3171.
46 P. Hohenberg and W. Kohn, Inhomogeneous Electron Gas, *Phys. Rev.*, 1964, **136**, B864–B871.
47 J. P. Perdew, K. Burke and M. Ernzerhof, Generalized Gradient Approximation Made Simple, *Phys. Rev. Lett.*, 1996, **77**, 3865–3868.
48 W. Kohn and L. J. Sham, Self-Consistent Equations Including Exchange and Correlation Effects, *Phys. Rev.*, 1965, **140**, A1133–A1138.
49 G. Kresse and D. Joubert, From ultrasoft pseudopotentials to the projector augmented-wave method, *Phys. Rev. B: Condens. Matter Mater. Phys.*, 1999, **59**, 1758–1775.
50 S. Grimme, J. Antony, S. Ehrlich and H. Krieg, A consistent and accurate ab initio parametrization of density functional dispersion correction (DFT-D) for the 94 elements H-Pu, *J. Chem. Phys.*, 2010, **132**, 154104.
51 H. J. Monkhorst and J. D. Pack, Special points for Brillouin-zone integrations, *Phys. Rev. B: Solid State*, 1976, **13**, 5188–5192.
52 M. Yu and D. R. Trinkle, Accurate and efficient algorithm for Bader charge integration, *J. Chem. Phys.*, 2011, **134**, 064111.
53 D. Singh, S. K. Gupta, Y. Sonvane and I. Lukačević, Antimonene: a monolayer material for ultraviolet optical nanodevices, *J. Mater. Chem. C*, 2016, **4**, 6386–6390.
54 D. Singh, S. Chakraborty and R. Ahuja, Emergence of Si 2 BN Monolayer as Efficient HER Catalyst under Co-functionalization Influence, *ACS Appl. Energy Mater.*, 2019, **2**, 8441–8448.
55 H. R. Mahida, *et al.* The influence of edge structure on the optoelectronic properties of Si 2 BN quantum dot, *J. Appl. Phys.*, 2019, **126**, 233104.
56 A. N. Andriotis, E. Richter and M. Menon, Prediction of a new graphenelike Si2BN solid, *Phys. Rev. B*, 2016, **93**, 2–4.
57 V. Shukla, R. B. Araujo, N. K. Jena and R. Ahuja, The curious case of two dimensional Si2BN: A high-capacity battery anode material, *Nano Energy*, 2017, **41**, 251–260.
58 D. Singh, S. K. Gupta, Y. Sonvane and R. Ahuja, High performance material for hydrogen storage: Graphenelike Si2BN solid, *Int. J. Hydrogen Energy*, 2017, **42**, 22942–22952.
59 K. Chang, *et al.*, MoS 2 /Graphene Cocatalyst for Efficient Photocatalytic H 2 Evolution under Visible Light Irradiation, *ACS Nano*, 2014, **8**, 7078–7087.
60 M. Guo, *et al.*, Edge dominated electronic properties of MoS 2 /graphene hybrid 2D materials: edge state, electron coupling and work function, *J. Mater. Chem. C*, 2017, **5**, 4845–4851.
61 K. F. Mak, C. Lee, J. Hone, J. Shan and T. F. Heinz, Atomically Thin <math display="inline"> <msub> <mi>MoS</mi> <mn>2</mn> </msub> </math> : A New Direct-Gap Semiconductor, *Phys. Rev. Lett.*, 2010, **105**, 136805.
62 W. Li, M. Guo, G. Zhang and Y.-W. Zhang, Edge-Specific Au/ Ag Functionalization-Induced Conductive Paths in Armchair MoS 2 Nanoribbons, *Chem. Mater.*, 2014, **26**, 5625–5631.
63 H. Pan and Y.-W. Zhang, Edge-dependent structural, electronic and magnetic properties of MoS2 nanoribbons, *J. Mater. Chem.*, 2012, **22**, 7280.

64 Y. Li, *et al.* MoS 2 Nanoparticles Grown on Graphene: An Advanced Catalyst for the Hydrogen Evolution Reaction, *J. Am. Chem. Soc.*, 2011, **133**, 7296–7299.

65 X. Li, L. Zhang, X. Zang, X. Li and H. Zhu, Photo-Promoted Platinum Nanoparticles Decorated MoS 2 @Graphene Woven Fabric Catalyst for Efficient Hydrogen Generation, *ACS Appl. Mater. Interfaces*, 2016, **8**, 10866–10873.

66 Q. Xiang, J. Yu and M. Jaroniec, Synergetic Effect of MoS 2 and Graphene as Cocatalysts for Enhanced Photocatalytic H 2 Production Activity of TiO 2 Nanoparticles, *J. Am. Chem. Soc.*, 2012, **134**, 6575–6578.

67 L. David, R. Bhandavat and G. Singh, MoS 2 /Graphene Composite Paper for Sodium-Ion Battery Electrodes, *ACS Nano*, 2014, **8**, 1759–1770.

68 Y. Chen, *et al.* Insights into the mechanism of the enhanced visible-light photocatalytic activity of black phosphorus/BiVO 4 heterostructure: a first-principles study, *J. Mater. Chem. A*, 2018, **6**, 19167–19175.